Effect of Calcium on Two-Dimensional Morphology and Photocatalytic Properties of Tin Oxide Nanoparticles

S. Vallimeena[*] and B. Helina

Department of Physics, St. Xavier's College (Autonomous) (Affiliated to Manonmaniam Sundaranar University, Tirunelveli), Palayamkottai-627002, India

*Corresponding author: E-mail: valliabhi11@gmail.com

A simple, inexpensive and environmental friendly co-precipitation approach has been used to synthesize calcium doped SnO_2 photocatalysts effectively with a high surface area. The X-ray diffraction (XRD), scanning electron microscopy (SEM), Raman spectroscopy, Fourier transform infrared (FTIR), ultraviolet-visible (UV-Vis) and photoluminescence (PL) spectroscopies all have been used to characterize the structural, morphological, optical and electrochemical properties of the prepared SnO_2:Ca nanoparticles. Both crystallized SnO_2 and SnO_2:Ca nanoparticles have tetragonal geometry. The structure and defects of the prepared sample were verified by the Raman spectra. The redshift in optical investigations confirmed the reduction in the optical band gap with increasing Ca content. The photocatalytic decomposition of methylene blue were also carried out using prepared SnO_2:Ca nanoparticles in visible light. In particular, when compared to other samples, the SnO_2:Ca (7 wt.%) nanoplates show the best photocatalytic activity which is confirmed from the low photoluminescence spectrum. By evenly dispersing Ca atoms across the SnO_2 matrix, the band gap may be significantly lowered, allowing for more effective separation of photogenerated electron-hole pairs and, in turn, more visible-light absorption. The charge separation efficacy of SnO_2:Ca (7 wt.%) nanoplates has been confirmed by EIS measurements.

Keywords: Calcium, Nanoplates, Photocatalytic degradation, Electrochemical studies.

INTRODUCTION

The rapid growth of the industrial society has resulted in issues such organic pollutants released into the ecosystem, which cause a serious threat to human health. Several traditional methods have been extensively investigated, but they are not cost-effective and do not guarantee complete removal of the toxic pollutant [1]. The best method for treating effluents has been found to be photocatalysis, since it has a great oxidative capacity against pollutants, is inexpensive and produces no toxic byproducts [2].

Numerous semiconductor photocatalysts for the degradation of hazardous pollutants, including ZnO, TiO_2, ZnS, SnS_2, *etc.* have been reported time to time [3]. The photocatalytic activity will increase due to the effective generation of photo-induced electron-hole pairs with a short bandgap and low recombination rate [4]. Among these possible catalysts, SnO_2 stands out as a fascinating and auspicious substance since

its high photoactivity, low cost and lack of toxicity [5,6]. The physical and chemical properties of SnO_2 has unique photocatalytic characteristics. Synthesis settings and post-calcination conditions may affect these features [6]. SnO_2 produces electron (e^-)-hole (h^+) pairs that reduce and oxidize surface adsorbates by using the radical species such as $OH^\bullet$ and $O_2^{-\bullet}$ [7].

However, nanostructured SnO_2 material has limitations in certain fields. Fast recombing of photogenerated e^--h^+ pairs and a large bandgap (3.6 eV) between the filled O_{2p} valence band (VB) and the Sn positions over the conduction band (CB) bottom reducing the efficiency of photocatalytic activity [8]. Recently, several strategies for overcoming the aforementioned issues *via* doping with additional metals have been proposed [9]. As a result, light absorption may be widened from UV to visible light while also increasing surface area. As a result of its high electron mobility (240 cm^2/Vs) and higher potential conduction band (CB), SnO_2 is a promising material for a wide variety of applications, including gas sensing, photocatalysis,

hydrogen generation, solar cells, supercapacitors, lithium-ion battery electrodes, optoelectronic devices, transparent conducting electrodes, and even state-of-the-art medical applications, such as cancer treatment and disease diagnosis [10].

By combining alkaline metals with SnO_2, the following characteristics can occur (i) the energy gap is altered and improve the electronic appearances which boost photocatalytic action, (ii) it causes lattice defects like oxygen vacancies and the production of ROS enhances the photocatalytic efficiency [11], (iii) alkaline (Mg, Ca, Sr, Ba) doped SnO_2 has high thermal steadiness [12], and (iv) calcium ions could inhabit substitutional positions in the SnO_2 matrix or become separated at grain boundaries. Bigger ionic radius of Ca^{2+} (1.14 Å) than Sn^{4+} (0.83 Å) proposes an insignificant replacement of Ca^{2+} ions in the SnO_2 matrix [13]. Calcium-loaded tin oxide sensors [14], alkaline earth metal (Mg, Ca, Sr, Ba) doped SnO_2 hollow nanospheres as a novel oxygen storage material [12], Ca and Pt catalyzed thin film SnO_2 gas sensors for CO and CO_2 detection [15], Ca, Sr and Ba on the structure, morphology and electrical properties of (Co, Sb)-doped SnO_2 varistors [16] and alkaline earth metals (Ba^{2+}, Ca^{2+} and Mg^{2+}) doped SnO_2 for visible light photocatalytic degradation [11] have been reported.

Ca doped SnO_2 nanoparticles have been prepared by precipitation method [11], solvothermal route [12], sonochemical method [14], *etc*. The simple chemical co-precipitation method is amenable to controlling the surface morphology, crystalline phase and grain size of the prepared nanoparticles [17]. In this study, SnO_2 and SnO_2:Ca nanoparticles were synthesized and the effect of Ca dopant on the structural, optical, morphological and photocatalytic activities of SnO_2 nanoparticles was investigated.

EXPERIMENTAL

Tin chloride, calcium acetate hydrate, centyl trimethylammonium bromide (CTAB) and ammonia solution provided by Sigma-Aldrich were used for preparing SnO_2 and SnO_2:Ca nanoparticles. A solvent mixture of double-distilled water and ethanol (2:1 ratio) was utilized for sample synthesis.

Synthesis of SnO_2 and Ca doped SnO_2: Calcium acetate hydrate and tin chloride were dissolved in 90 mL of distilled water and ethanol. The aforementioned CTAB solution was then slowly infused with aqueous solution while being vigorously stirred. It was precipitated by the gradual addition of an ammonia solution. Calcination was used to get rid of organic stabilizer and the solvent medium. After 2 h annealing step at 500 ºC, SnO_2 and SnO_2:Ca-CTAB were crystallized. The obtained products were then sintered at 500 ºC for 2 h in an air environment. This technique ensured that no discernible impurity phase was occurred by mixing it at the atomic level.

Characterization: The morphology of the synthesized samples was examined by CAREL ZEISS, EVO 18. The X-ray diffraction (XRD) was used to analyze the structures of the prepared sample by employing $CuK\alpha$ ($\lambda = 1.5414$ Å) radiation as the X-ray source, with the incident angle fixed at 2θ and the scan range was from 20º to 80º. In this case, an FT-Raman spectrometer was used to analyze the Raman spectra (Bruker RFS 27). The vibrational analyses were inspected using a Fourier

transmission infrared spectrometer (FTIR-7600 Lambda Intelligent). The absorption spectrum (Lambda 35 model) were collected using a UV-Vis-NIR spectrophotometer. At an excitation wavelength of 330 nm, the photoluminescence spectra were analyzed using a spectroflurophotometer (Shimadzu RF-5301). The electrochemical impedance spectroscopy (EIS) readings were analyzed using the software programme Versastat MC-Metex.

Photocatalytic activities: The photocatalytic activity of the prepared nanoparticles was assessed for degrading methylene blue dye solution. SnO_2 and SnO_2:Ca nanoparticles (10 mg) were mixed with 100 mL of methylene blue dye solution. Visible light radiation was exploited as a source of illumination. For 30 min, the dye solution was kept in dark to verify adsorption-desorption equilibrium. The apparent absorption intensity of effluent was analyzed using Perkin-Elmer LAMBDA-35 spectrophotometer. The degradation efficiency of the dye was calculated using eqn. 1:

$$\text{Degradation efficiency } (\%) = \frac{C_o - C}{C_o} \times 100 \qquad (1)$$

where C_o and C represent the concentrations of the dye mixture in the effluent at time t = 0 and time t, respectively.

RESULTS AND DISCUSSION

XRD studies: All samples of SnO_2 and SnO_2:Ca nanoparticles comprised of tetragonal structure (JCPDS no. 880287) is shown in Fig. 1. The diffraction peaks of SnO_2:Ca nanoparticles at 2θ values of 26.6º, 33.9º, 37.9º, 51.8º, 54.9º, 57.7º, 61.9º and 64.9º can be associated with the crystallline plane of (110), (101), (200), (211), (220), (002), (310) and (112), respectively [18]. Since no impurity phase was observed, the final products produced under the current experimental conditions are highly pure. Broad peaks observed in diffraction patterns showed that the synthesized samples are nanocrystalline in nature. The CaO stabilizing the grain boundaries and prevents SnO_2 particles from developing during calcination, which in turn keeps the fine-grained structure intact and lowers the SnO_2 peak intensities [14]. The Scherrer's formula was used for calculating the crystallite size and their obtained value was 17 nm for SnO_2 and 10.03, 13.2 and 8.84 nm for 3, 5 and
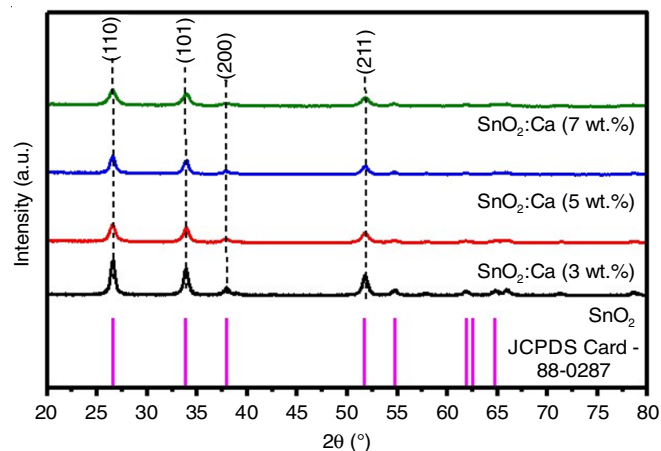

Fig. 1. XRD spectra of SnO_2:Ca nanoparticles

7 wt.% Ca doped SnO_2 nanoparticles, respectively. A reduction of the grain sizes due to the integration of Ca^{2+} impurities lead to the reduction in nucleation as well as hamper the growing of SnO_2 crystal [11].

Morphological studies: EDAX was used to study the elemental allocation of SnO_2:Ca and the consistent data of weight percentages are shown in insert of Fig. 2a-b. The EDAX spectrum validated the existence of Ca, Sn and O within the doped SnO_2 samples. Additionally, these spectra proved that the samples had no other components.

Fig. 3 depicts the surface morphology of SnO_2:Ca nanoparticles (0,3,5 and 7 wt.%) as examined by SEM. The SnO_2 and SnO_2: Ca (3 wt.%) nanoparticles exhibits the spherical shape (Fig. 3a-b), whereas SnO_2:Ca (5 wt.%) illustrates the irregular shape with small nanoparticles (Fig. 3c). The 2D square platelet shaped SnO_2:Ca (7 wt.%) nanoparticles are shown in Fig. 3d. The SnO_2:Ca (7 wt.%) nanoparticles are reinforced along (110) facets that hinder growth in different directions. On the other hand, the development of 2D square nanoplatelets of SnO_2:Ca (7 wt.%) may be ascribed to the capping ligands
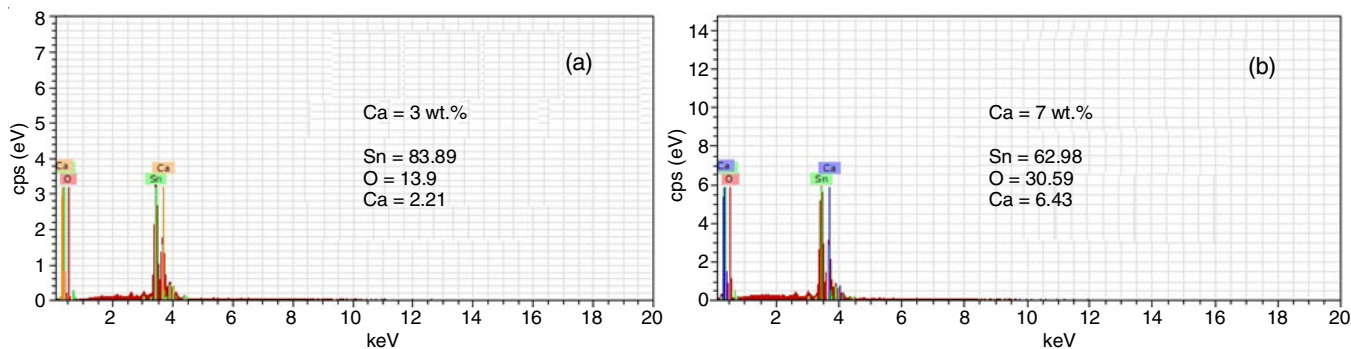

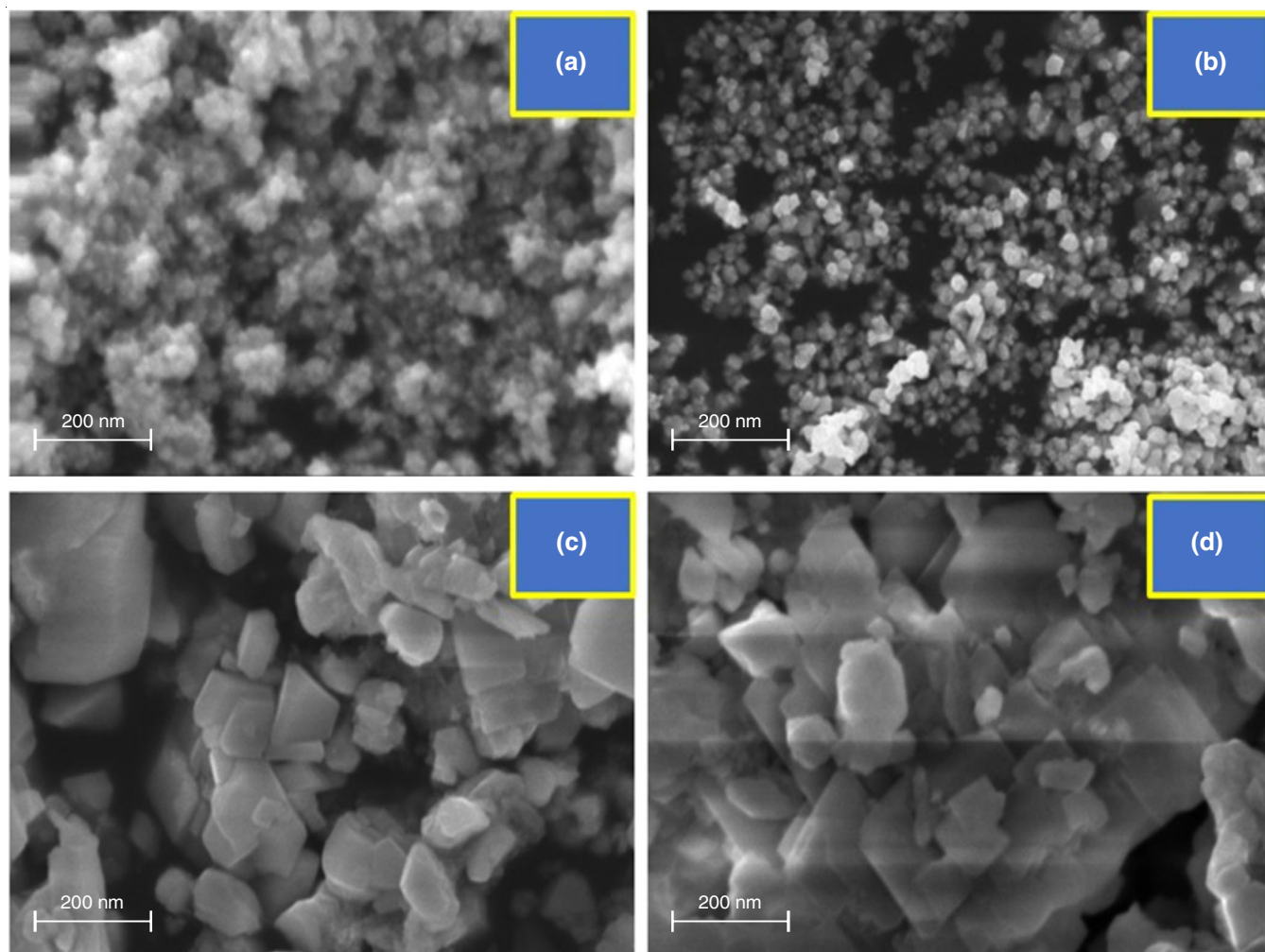Fig. 2. EDAX spectra of SnO_2:Ca nanoparticles

Fig. 3. SEM images of (a) undoped, (b) 3 wt.%, (c) 5 wt.% and (d) 7 wt.% Ca doped SnO_2 nanoparticles

(CTAB) template effect. It is concluded that the Ca doping influences the host SnO_2.

Raman studies: The Raman spectra of Ca doped SnO_2 nanoparticles is shown in Fig. 4. At the middle of first Brillouin zone, the normal vibration modes' mechanical representation is provided by $M = A_{1g} + A_{2g} + B_{1g} + B_{2g} + E_g + 2A_{2u} + 2B_{1u} + 4E_u$ [19]. The vibrational mode such as A_{1g}, B_{1g}, B_{2g} are non-degenerate vibrates perpendicular to *c*-axis and E_g doubly degenerate modes along the direction of the *c*-axis are Raman active and B_{1u} and A_{2g} modes are silent modes. The A_{2u} and triply degenerate E_u modes are IR active, whereas $2E_u$ and $1A_{2u}$ are acoustic modes [20]. The Sn atom remains in a rest location, while the O-atoms vibrate. The E_g, A_{1g} and B_{2g} are existed at 482, 631 and 778 cm^{-1}, respectively.
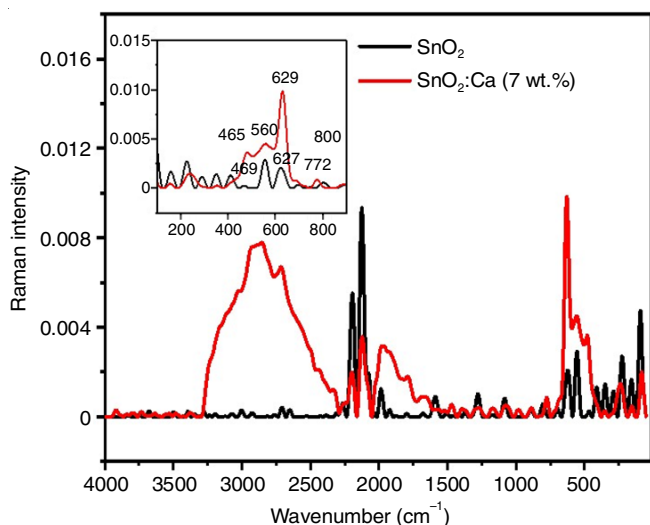

Fig. 4. Raman spectra of SnO_2:Ca nanoparticles

The zone center vibrations of bulk crystalline SnO_2 having tetragonal rutile form generate four Raman active peaks *viz.* A_{1g} (634 cm^{-1}), B_{2g} (773 cm^{-1}) and E_g (473 cm^{-1}) [21]. These active modes correlate well with the previously reported typical rutile tetragonal SnO_2 structure [11]. The non-degenerate A_{1g} and B_{2g} Raman modes represent the contraction and extension of the vibration of Sn-O links. The E_g mode is related to the oxygen plane vibration. When alkaline metal ions were added, there is a shift toward a higher wavenumber. Substitution of alkaline metals marginally modify the defect such as unoccupied lattice locations, which may lead to lattice distortion and a decrease in lattice space symmetry [22].

FTIR studies: The FTIR spectra of SnO_2 and SnO_2:Ca nanoparticles are displayed in Fig. 5. A band near 3442-3430 cm^{-1} is ascribed to the vibrational mode of O-H bonds, whereas narrow band at 1640-1631 cm^{-1} is due to the bending vibration of H_2O [23]. The peaks observed at 2937-2922 cm^{-1} and 1434-1393 cm^{-1} for SnO_2 and SnO_2:Ca, respectively indicates the CH_2 stretching of the CTAB [24] and C-H bending vibration, respectively. The FT-IR spectra bands at 1103 and 1051 cm^{-1} for SnO_2 and SnO_2:Ca are assigned toward C-O-C vibrating mode. The intense peak identified at 561-556 and 657-641 cm^{-1} concurrence the O-Sn-O and Sn-O lattice stretch, respectively [25]. To a greater extent than without doping, a peak of SnO_2
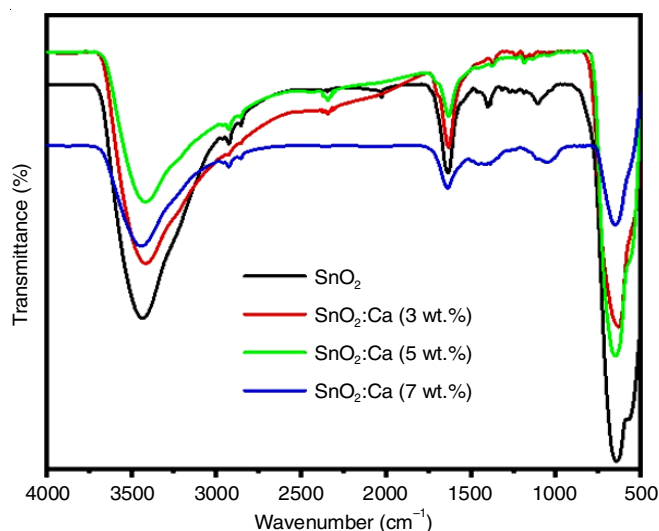

Fig. 5. FTIR spectra of SnO_2:Ca of nanoparticles

occurs at 561 cm^{-1} for SnO_2 gets shifted to 556 cm^{-1} for SnO_2: Ca (3 and 5 wt.%) and at higher concentration (Ca = 7 wt.%) it is reduced. The introduction of Ca^{2+} ions in the interstitial site leads to the widening and shifting of Sn-O-Sn and Sn-O modes. As Ca^{2+} ions impact the SnO_2 lattice more strongly than Sn^{4+} ions because of its greater ionic radii. The bands related to OH groups in the prepared samples indicate increased the photocatalytic activity and hinder electron-hole pair recombination [26].

Optical studies

UV-Vis DRS studies: The optical features of SnO_2 and Ca doped SnO_2 nanoparticles was determined by UV-Vis DRS. Fig. 6a shows that all the synthesized photocatalysts illustration the absorption wavelength in the UV region. Moreover, SnO_2:Ca nanoparticles revealed a red shifted than SnO_2 and which is similar to alkaline earth metals doped SnO_2 [11]. The absorption peaks of SnO_2 and SnO_2:Ca nanoparticles appear at 330 and 540 nm, which is caused by photon excited electrons (e^-) from the valence band (VB) to the conduction band (CB).

The band gap of the synthesized nanoparticles is calculated by Taucs plot and is shown in Fig. 6b. The bandgap energy was found to be 3.7, 3.51, 3.4 and 3.3 eV for pure SnO_2, 3 wt.%, 5 wt.% and 7 wt.% Ca doped SnO_2 nanoparticles, respectively. The decrease in band gap of Ca doped SnO_2 nanoparticles confirmed that Ca^{2+} ions were doped into the SnO_2 lattice. An increase in the conduction band (CB) of SnO_2:Ca (7 wt.%) nanoplates allows for several photogenerated e^- to combine with O_2 and create $O_2^{-\bullet}$ and also blocks the recombination of e-h^+ pairs [27].

Photoluminescence studies: The photoluminescence spectra of the SnO_2 and SnO_2:Ca nanoparticles are shown in Fig. 6c. Undoped SnO_2 revealed a violet and green emission at 445 and 507 nm. By comparing to undoped SnO_2, SnO_2:Ca exhibits emission peaks at 360, 395, 466 and 518 nm. The UV emission peaks exists at 360 and 395 nm are associated with near band edge emissions of excitons and which is analogous to the work of Asaithambi *et al.* [11] regarding the alkaline earth metals doped SnO_2. The appearance of new peak on SnO_2:
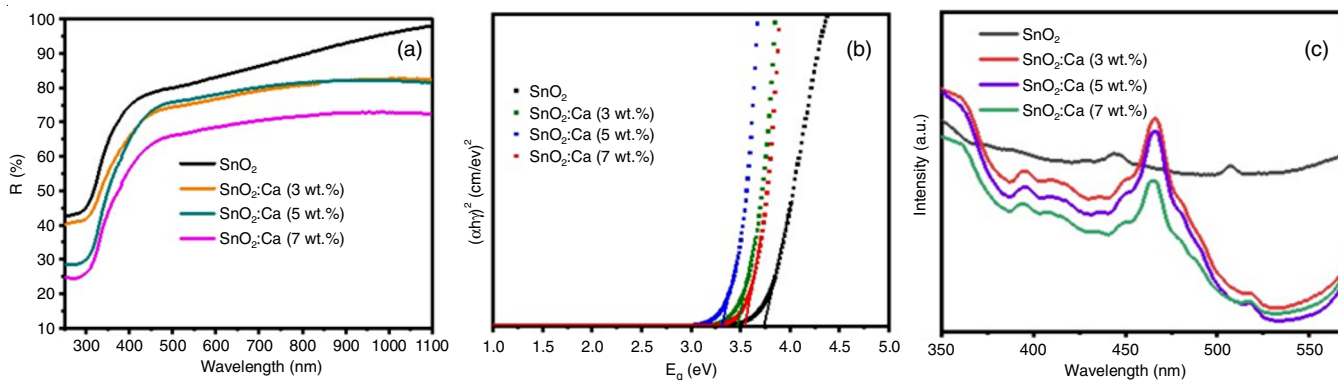
Fig. 6. (a) UV-vis diffuse reflectance spectra, (b) Taucs plot and (c) PL spectra of SnO_2 and SnO_2:Ca nanoparticles

Ca nanoparticles proposes an augment in oxygen vacancies [28]. Blue emission peak observed at 466 nm is due to the structural defects and electron recombination with shallow level defects [29]. The weak green emission peak, appearing at 520 nm, corresponds to the singly ionized oxygen vacancies [30]. Increasing the Ca dopant intensifies the non-radiative transition. Since these defect energy levels are inside the band gap of SnO_2, may account for the observed emissions at longer wavelength [31].

The most prevalent defects in oxides are oxygen vacancies, which typically operate as radiative centers in the luminescence action. The photons emission at 390 nm is related to the existence of VO^+ (neutral oxygen vacancies) in SnO_2 matrix, which can be transformed into ionized vacancies [31,32]. The other two wide peaks may be as a result of univalent ($VO^\bullet$) and bivalent ($VO^{\bullet\bullet}$) positive charged oxygen vacancies and which energy levels are situated within the band gap. In actual fact, Ca^{2+} is incorporated to Sn^{4+}, an oxygen ion location remains left unoccupied for maintaining the 1:2 cation and anion affiliation site. With Kroger-Vink equation, it could be represented as [14]:

$$CaO(s) + SnO_2 \longrightarrow Ca''_{Sn} + O^x + VO^{\bullet\bullet}$$
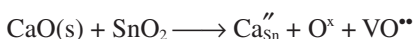
As observed from the PL spectra, calcium doping increased the oxygen vacancies in SnO_2 up to the solubility limit. Typically, a low intensity of PL emission presumes a low recombination of excited electrons and holes, which enables the production of a large number of $^\bullet OH$ radicals to enhance the photocatalytic degradation [26].

Electrochemical studies: The Nyquist plot and their equivalent circuit of SnO_2:Ca nanoparticles are displayed in Figs. 7 and 8, respectively. Fig. 8 shows that SnO_2:Ca (7 wt.%)
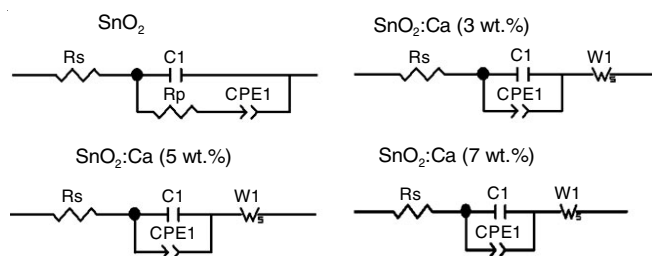

Fig. 7. Correspondent circuit utilized for fitting data of SnO_2:Ca nanoparticles

demonstrated lesser arc radius in the EIS Nyquist plots compared to other samples. It is suggested that SnO_2:Ca (7 wt.%) had lower interfacial layer resistance and therefore faster e^-–h^+ pairs transfer also separating efficacy [32]. In addition, the SnO_2:Ca (7 wt.%) nanoplate shows the smallest semicircle in the higher frequency zone, representing that 7 wt.% Ca doped electrode has a low charge transmission resistance. Since, the existence of Ca^{2+} in SnO_2 increases charge carrier passage.

Photocatalytic degradation

Influence of SnO_2:Ca nanoparticles: The influence of dopant concentration on the photocatalytic action of SnO_2 nanoparticles was determined by analyzing alterations in the optical absorption characteristics of aqueous methylene blue dye *via* photodegradation. Fig. 9a-d illustrates the photodegradation of methylene blue dye in SnO_2 and SnO_2:Ca samples (2 h). The absorption spectra of methylene blue dye exhibited a high absorption peak at 664 nm, which was attributed to a chromophore. When the exposure duration to visible light was increased from 30 to 120 min, it was found that all the absorption peaks were progressively weaker, indicating that the catalyst acted to break down the methylene blue chromophore in addition to the aromatic ring and their decomposed products.

The primary absorption band was nearly disappeared and the colour of methylene blue solution had disappeared within 120 min, indicating a more thorough mineralization of methylene blue by SnO_2:Ca (7 wt.%) nanoplates. Typically, degradation does not produce any new peaks in the absorption spectrum. It clearly indicates that SnO_2:Ca (7 wt.%) nanoplates exhibited the best photocatalytic activity (degraded 83%) by comparing with other samples such as SnO_2, SnO_2:Ca (3 and 5 wt.%), which were 66%, 68% and 71%, respectively. The efficiency of SnO_2:Ca photocatalyst compared with SnO_2 based nanoparticles are displayed in Table-1.

Several distinct parameters, including morphology, particle size, absorbency, crystallinity and surface area, can affect the enhancement of photodegradation performance [33]. High surface area might offer additional photodegradation reaction active sites and boost the effectiveness of the e^--h^+ split-up [5]. Furthermore, compared to other morphologies, the photocatalytic degradation of nanoplatelet 2D structures with lower band gap energies of SnO_2:Ca (7 wt.%) was higher.
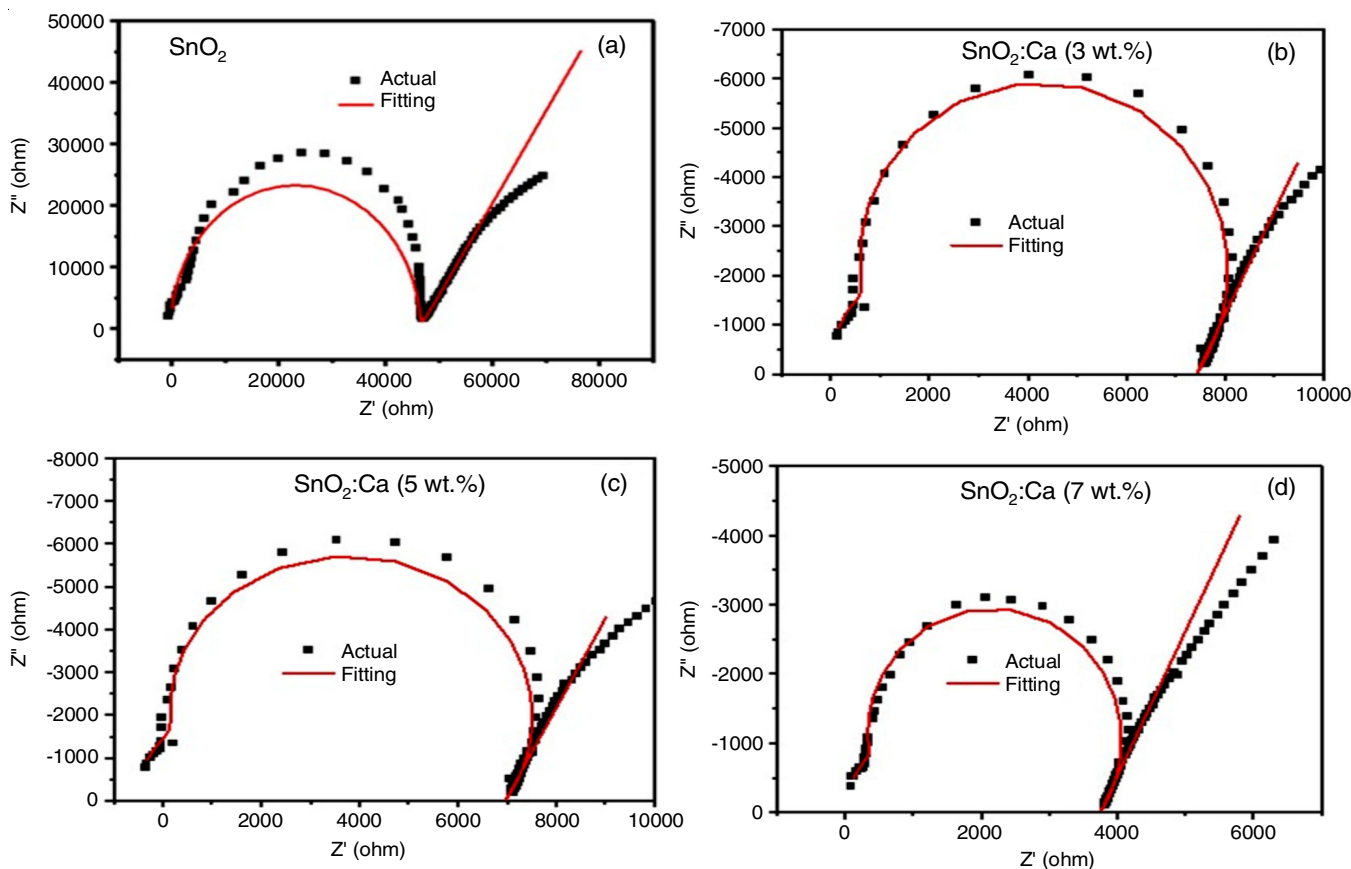
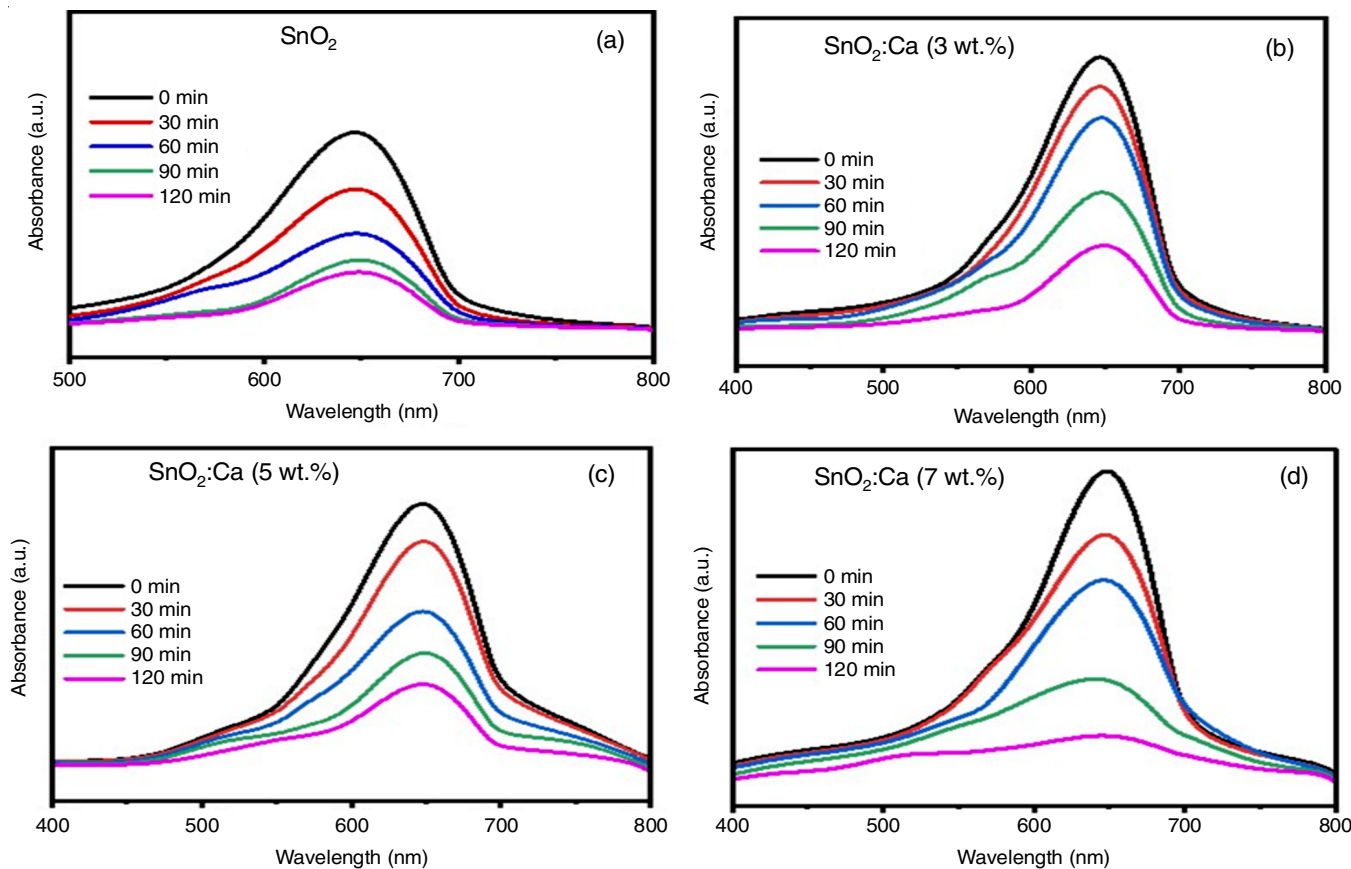Fig. 8. Impedance curves of SnO$_2$:Ca nanoparticles

Fig. 9. Absorbance spectra of methylene blue dye in the presence of SnO$_2$:Ca nanoparticles
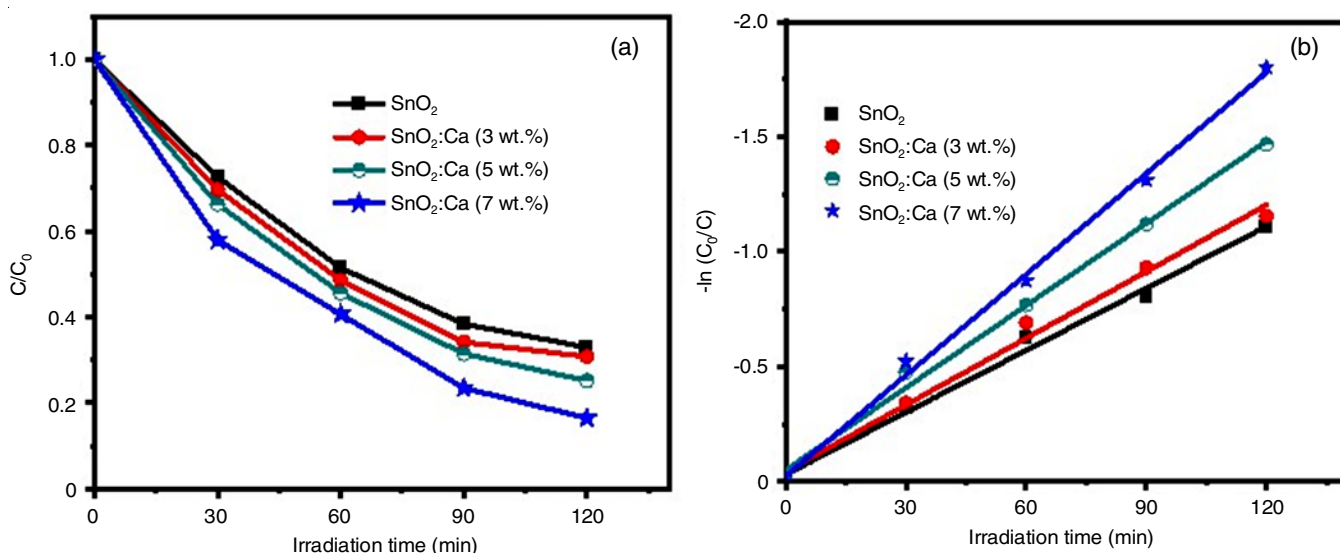
Fig. 10. (a) Plots of (C/C_0) and (b) $-\ln(C_0/C)$ against irradiation time for SnO_2:Ca nanoparticles

TABLE-1
DEGRADATION EFFICIENCY (%), REGRESSION
COEFFICIENT (R^2) AND RATE CONSTANT (k)
OF THE SnO_2:Ca NANOPARTICLES

Sample	MB dye (120 min)		
	Degradation efficiency (%)	R^2	K
SnO_2	66	0.95220	0.008931
SnO_2:Ca (3 wt.%)	68	0.98920	0.009670
SnO_2:Ca (5 wt.%)	71	0.99420	0.011920
SnO_2:Ca (7 wt.%)	83	0.99674	0.014640

Kinetic study: As stated by the Langmuir–Hinshelwood kinetics model the degrading rate constant of the synthesized SnO_2:Ca nanoparticles was measured by the constant rate reckoning $\ln (C_0 - C_t) = kt$, where k is the rate constant and C_0, C_t are the before and final absorption of methylene blue dye subsequently at time t, respectively. The photodegradation process obeys the pseudo-first-order kinetics as a result of the photocatalytic reaction illustrates the straight relationship. A graph between $\ln(C_0/C_t)$ and irradiation time is revealed in Fig. 10b. When Ca dopant concentration is increased, k value also increased from 0.008931 to 0.01464 min^{-1}. The SnO_2:Ca (7 wt.%) nanoplates has a highest k value than other photocatalysts.

Proposed mechanism: The capture of e^- from the CB of SnO_2 by photocatalytic activity when Ca is added to SnO_2 lowers the possibility of charge recombination. Additionally, it produces oxygen vacancies and facilitates charge carrier separation. Moreover, the photocatalyst's broad surface area encourages higher organic contaminant adsorption on its surface, which may increase photocatalytic activity [34]. When SnO_2 is exposed to light, it absorbs light equivalent to or more than its band gap, causing an e^- to be moved from the VB to the CB. Recombination of $e^- - h^+$ pairs was reduced, e^- and h^+ can readily travel to the photocatalysts surface and it may participate in redox reactions with adsorbed species. The detached holes existing in the VB of SnO_2 can reduce the H_2O to produce hydroxyl radical (OH$^\bullet$) and concurrently, the

bandgap of SnO_2 is reduced by Ca ions to generate reactive superoxide radicals($O_2^{\bullet-}$), which then convert into OH$^\bullet$ over electron reduction paths as shown in Fig. 11.
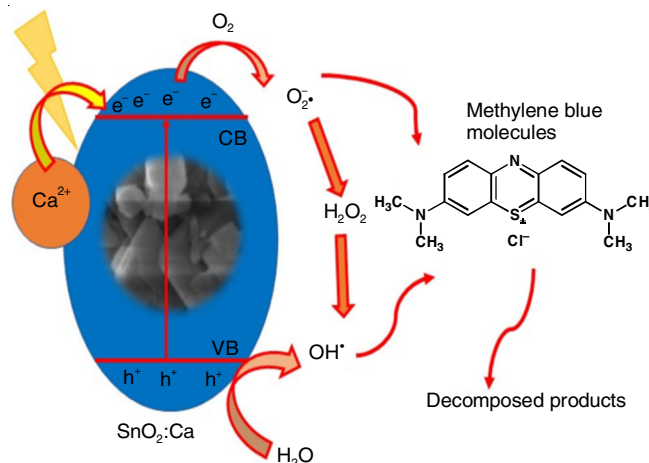

Fig. 11. Photocatalytic mechanism of SnO_2:Ca nanoplates

Conclusion

The 2D SnO_2:Ca nanoplates were prepared *via* a facile precipitation method. CTAB acted as a morphology and structure capping agent, thus increasing the surface area and enhancing the photocatalytic activity under visible light. The obtained SnO_2:Ca (7 wt.%) nanoplates showed higher photocatalytic degrading of methylene blue dye than undoped SnO_2. Electrochemical analysis divulged that the higher photocatalytic activity of SnO_2:Ca (7 wt.%) nanoplates is due to the improvement of the charge transmission and separating efficacy. The lowest intensity of photoluminescence emission suggests the less recombination of excited electrons and holes as a significant prompting feature for the photocatalytic elimination of methylene blue dye. This study providing a simple calcium doped approach for preparing SnO_2:Ca effective photocatalyst for decomposing organic impurities.

ACKNOWLEDGEMENTS

CONFLICT OF INTEREST

The authors declare that there is no conflict of interests regarding the publication of this article.

REFERENCES

1. S. Sharma and S. Basu, *Sep. Purif. Technol.*, **231**, 115916 (2020);
    https://doi.org/10.1016/j.seppur.2019.115916

2. J. Xu, Z. Wang and Y. Zhu, *ACS Appl. Mater. Interfaces*, **9**, 27727 (2017);
    https://doi.org/10.1021/acsami.7b07657

3. D. Monga, S. Sharma, N.P. Shetti, S. Basu, K.R. Reddy and T.M. Aminabhavi, *Mater. Today Chem.*, **19**, 100399 (2021);
    https://doi.org/10.1016/j.mtchem.2020.100399

4. A. Kundu, S. Sharma and S. Basu, *J. Phys. Chem. Solids*, **154**, 110064 (2021);
    https://doi.org/10.1016/j.jpcs.2021.110064

5. A. Sadeghzadeh-Attar, *Sol. Energy Mater. Sol. Cells*, **183**, 16 (2018);
    https://doi.org/10.1016/j.solmat.2018.03.046

6. P. Manjula, R. Boppella and S.V. Manorama, *ACS Appl. Mater. Interfaces*, **4**, 6252 (2012);
    https://doi.org/10.1021/am301840s

7. M. Batzill, *Energy Environ. Sci.*, **4**, 3275 (2011);
    https://doi.org/10.1039/c1ee01577j

8. S. Vadivel and G. Rajarajan, *J. Mater. Sci. Mater. Electron.*, **26**, 7127 (2015);
    https://doi.org/10.1007/s10854-015-3335-2

9. S.K. Jain, M. Fazil, F. Naaz, N.A. Pandit, J. Ahmed, S.M. Alshehri, Y. Mao and T. Ahmad, *New J. Chem.*, **46**, 2846 (2022);
    https://doi.org/10.1039/D1NJ05432E

10. A.H. Pinto, A.E. Nogueira, C.J. Dalmaschio, I.N. Frigini, J.C. de Almeida, M.M. Ferrer, O.M. Berengue, R.A. Gonçalves and V.R. de Mendonça, *Solids*, **3**, 327 (2022);
    https://doi.org/10.3390/solids3020024

11. S. Asaithambi, P. Sakthivel, M. Karuppaiah, Y. Hayakawa, A. Loganathan and G. Ravi, *Appl. Phys., A Mater. Sci. Process.*, **126**, 265 (2020);
    https://doi.org/10.1007/s00339-020-3441-8

12. Q. Dong, S. Yin, M. Yoshida, X. Wu, B. Liu, A. Miura, T. Takei, N. Kumada and T. Sato, *Mater. Res. Bull.*, **69**, 116 (2015);
    https://doi.org/10.1016/j.materresbull.2014.11.018

13. B.K. Min and S.D. Choi, *Sens. Actuators B Chem.*, **99**, 288 (2004);
    https://doi.org/10.1016/j.snb.2003.11.025

14. S. Ghosh, M. Narjinary, A. Sen, R. Bandyopadhyay and S. Roy, *Sens. Actuators B Chem.*, **203**, 490 (2014);
    https://doi.org/10.1016/j.snb.2014.06.111

15. K. Steiner, U. Hoefer, G. Kuhner, G. Sulz and E. Wagner, *Sens. Actuators B Chem.*, **25**, 529 (1995);
    https://doi.org/10.1016/0925-4005(95)85114-3

16. J.A. Aguilar-Martínez, E. Rodríguez, S. Garcia-Villarreal, L. Falcon-Franco and M.B. Hernández, *Mater. Chem. Phys.*, **153**, 180 (2015);
    https://doi.org/10.1016/j.matchemphys.2015.01.001

17. M. Karuppaiah, P. Sakthivel, S. Asaithambi, R. Murugan, R. Yuvakkumar and G. Ravi, *Mater. Chem. Phys.*, **228**, 1 (2019);
    https://doi.org/10.1016/j.matchemphys.2019.02.034

18. A.K. Sekone, Y.-B. Chen, M.-C. Lu, W.-K. Chen, C.-A. Liu and M.-T. Lee, *Nanoscale Res. Lett.*, **11**, 1 (2016);
    https://doi.org/10.1186/s11671-015-1209-4

19. A. Diéguez, A. Romano-Rodríguez, A. Vilà and J.R. Morante, *J. Appl. Phys.*, **90**, 1550 (2001);
    https://doi.org/10.1063/1.1385573

20. P. Sangeetha, V. Sasirekha and V. Ramakrishnan, *J. Raman Spectrosc.*, **42**, 1634 (2011);
    https://doi.org/10.1002/jrs.2919

21. M. Karmaoui, A.B. Jorge, P.F. McMillan, A.E. Aliev, R.C. Pullar, J.A. Labrincha and D.M. Tobaldi, *ACS Omega*, **3**, 13227 (2018);
    https://doi.org/10.1021/acsomega.8b02122

22. J. Kaur, J. Shah, R.K. Kotnala and K.C. Verma, *Ceram. Int.*, **38**, 5563 (2012);
    https://doi.org/10.1016/j.ceramint.2012.03.075

23. N. Chen, B. Liu, P. Zhang, C. Wang, Y. Du, W. Chang and W. Hong, *Inorg. Chem. Commun.*, **132**, 108848 (2021);
    https://doi.org/10.1016/j.inoche.2021.108848

24. R.A. Campbell, S.R. Parker, J.P. Day and C.D. Bain, *Langmuir*, **20**, 8740 (2004);
    https://doi.org/10.1021/la048680x

25. A.B. Ali Baig, V. Rathinam and J. Palaninathan, *Appl. Water Sci.*, **10**, 1 (2020);
    https://doi.org/10.1007/s13201-019-1058-x

26. S. Nachimuthu, S. Thangavel, K. Kannan, V. Selvakumar, K. Muthusamy, M.R. Siddiqui, S.M. Wabaidur and C. Parvathiraja, *Chem. Phys. Lett.*, **804**, 139907 (2022);
    https://doi.org/10.1016/j.cplett.2022.139907

27. J. Liu, W. Lu, Q. Zhong, X. Jin, L. Wei, H. Wu, X. Zhang, L. Li and Z. Wang, *Mol. Catal.*, **433**, 354 (2017);
    http://dx.doi.org/10.1016/j.mcat.2017.02.033

28. J. Yan, B. Jin, P. Zhao and R. Peng, *Inorg. Chem. Front.*, **8**, 777 (2021);
    https://doi.org/10.1039/D0QI01218A

29. V. Kumar, Bhawna, S.K. Yadav, A. Gupta, B. Dwivedi, A. Kumar, P. Kumar and K. Deori, *ChemistrySelect*, **4**, 3722 (2019);
    https://doi.org/10.1002/slct.201900032

30. F.E. Ghodsi and J. Mazloom, *Appl. Phys., A Mater. Sci. Process.*, **108**, 693 (2012);
    https://doi.org/10.1007/s00339-012-6952-0

31. X. Li, F. Li and Y. Xie, Trends in Water Pollution Research, Nova Science Publishers, New Delhi, India, pp. 31-74 (2005).

32. A.R. Babar, S.S. Shinde, A.V. Moholkar, C.H. Bhosale, J.H. Kim and K.Y. Rajpure, *J. Semicond.*, **32**, 053001 (2011);
    https://doi.org/10.1088/1674-4926/32/5/053001

33. A.H. Mamaghani, F. Haghighat and C.-S. Lee, *Appl. Catal. B*, **203**, 247 (2017);
    https://doi.org/10.1016/j.apcatb.2016.10.037

34. S. Wu, H. Cao, S. Yin, X. Liu and X. Zhang, *J. Phys. Chem. C*, **113**, 17893 (2009);
    https://doi.org/10.1021/jp9068762